J. Fluid Mech. (2021), *vol*. 915, A108, doi:10.1017/jfm.2021.101

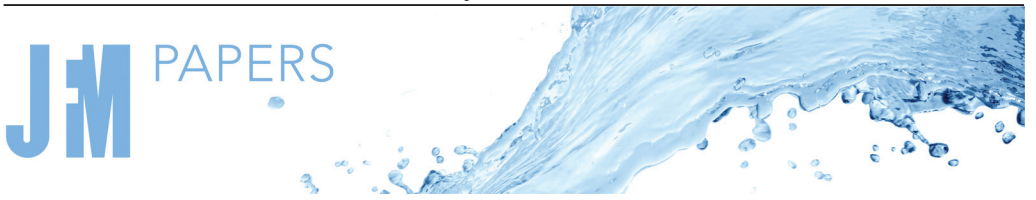

Acoustic–gravity waves from multi-fault rupture

Byron Williams[1], **Usama Kadri**[1,†] **and Ali Abdolali**[2,3,4]

[1]School of Mathematics, Cardiff University, Cardiff CF24 4AG, UK

[2]NWS/NCEP/Environmental Modeling Center, National Oceanic and Atmospheric Administration (NOAA), College Park, MD 20740, USA

[3]I.M. Systems Group, Inc. (IMSG), Rockville, MD 20852, USA

[4]University of Maryland, College Park, MD 20742, USA

(Received 4 March 2020; revised 25 July 2020; accepted 26 January 2021)

The propagation of wave disturbances from a complex multi-fault submarine earthquake of slender rectangular segments in a sea of constant depth is discussed, accounting for both water compressibility and gravity effects. It is found that including gravity effects the modal envelopes of the modified two-dimensional acoustic waves and the tsunami are governed by the Schrödinger equation. An explicit solution is derived using a multi-fault approach that allows capturing the main peak of the tsunami. Moreover, a linear superposition of the solution allows solving complicated multi-fault ruptures, in particular in the absence of dissipation due to large variations in depth. Consequently, the modulations of acoustic waves due to gravity, and of tsunami due to compressibility, are governed simultaneously and accurately, which is essential for practical applications such as tsunami early warning systems. The results are validated numerically against the mild-slope equation for weakly compressible fluids.

Key words: slender-body theory

1. Introduction

Tsunamis have a long history of devastation, costing the lives of thousands of people, causing damage to property and posing a continuing threat to thousands of kilometres of shoreline. In the last two decades, we have witnessed the deadliest 2004 Sumatra earthquake and tsunami, followed by other major (tsunamigenic) earthquakes, such as the 2011 Tohoku Oki, and, more recently, the 2018 Sulawesi and Palu tsunami. These have repeatedly proven that a primary reason for the scale of devastation is the failure to provide a reliable early warning. Current warning systems rely heavily on DART buoys (Deep ocean Assessment and Reporting of Tsunamis) and seismic measurements.

† Email address for correspondence: kadriu@cardiff.ac.uk

Accurate tsunami evaluation from DART buoys may be possible, though depending on particular circumstances there may not be sufficient time for early warning. On the other hand, seismic data provide valuable information on the tectonic movements, earthquake size and possible epicentre, though with current technology and analysis they fail to assess the tsunami threat. A complimentary approach has been suggested by a number of authors who considered the slight compressibility of the water in their analysis (Miyoshi 1954; Sells 1965; Yamamoto 1982; Nosov 1999; Stiassnie 2010; Kadri & Stiassnie 2012, 2013*b*; Cecioni *et al.* 2014; Kadri 2015; Abdolali *et al.* 2018). In this approach, attention is focused on acoustic–gravity waves that radiate from submarine earthquakes alongside the tsunami, and propagate through the liquid or elastic layers (Eyov *et al.* 2013; Kadri 2016). Acoustic–gravity waves are compression waves that reside within the entire water column and can couple with the elastic sea bottom. They carry information about the source at relatively high speeds ranging from the speed of sound in water (1500 ms^{-1}) to Rayleigh waves speed in the solid (3200 ms^{-1}) that far exceed the phase speed of the tsunami (200 ms^{-1} at 4 km water depth), see Eyov *et al.* (2013). In the solid layer, compression P (pressure) waves and S (shear) waves propagate at approximately 6800 and 3900 ms^{-1}, respectively (e.g. see preliminary earth reference model table 1 of Dziewonshi & Anderson 1981). A critical difference between analysing acoustic–gravity waves and P and S waves is that the former, being a compression wave in the liquid layer, is directly associated with the effective vertical uplift. Hence, acoustic–gravity waves can not only act as excellent precursors, but they could also provide vital information on the geometry and dynamics of the effective uplift, which eventually shapes the main characteristics of the tsunami. Note that sea-bottom elasticity can significantly affect the phase speed of acoustic–gravity waves but only in shallow water (Eyov *et al.* 2013; Kadri 2019). On the other hand, water compressibility and sea-bottom elasticity affect the phase speed of surface gravity waves and should be considered when accurate transoceanic tsunami modelling is sought (Abdolali & Kirby 2017; Abdolali, Kadri & Kirby 2019). The peak frequency shift and attenuation of acoustic–gravity waves takes place due to interaction with a visco-elastic sedimentary layer at the sea bottom (Abdolali, Kirby & Bellotti 2015*b*; Prestininzi *et al.* 2016).

The possibility of using the acoustic forerunner as an early warning signal has long been established (Yamamoto 1982; Nosov 1999; Stiassnie 2010; Kadri & Stiassnie 2013*a*; Renzi & Dias 2014; Abdolali *et al.* 2015*a*; Kadri 2015, 2016; Kadri & Akylas 2016). Finite fault models have also been investigated, providing a three-dimensional theory of acoustic–gravity waves based on the classical method of the Green's function (Hendin & Stiassnie 2013). However, their utility in providing predictions for acoustic and surface wave behaviour in real time is limited. The limitation arises due to the solution being in integral form which requires partitioning of any shape considered into many small elements, calculating the contribution from each element, then performing a summation to arrive at the total contribution. In the absence of an explicit analytical solution, this proves to be computationally expensive (Mei & Kadri 2018) and, of course, the processing burden escalates with the addition of more complex multi-fault ruptures, as observed in nature (Hamling *et al.* 2017). An alternative approach was proposed by Mei & Kadri (2018) who considered a slender fault and invoked multiple scales analysis to obtain a closed-form analytical solution for the propagating acoustic modes. Improvements in long-range modulation are provided by the introduction of envelope factors involving Fresnel integrals. Moreover, an inverse approach was employed and relations for fault location and rupture parameters were derived. Further developments of the inverse approach can be found in Bernabe & Usama (2021).

There are two main objectives of the present work. The first is to extend the results of Mei & Kadri (2018) to include gravitational effects and multi-fault ruptures. The inclusion of gravitation involves a modification to the surface-boundary condition. This modification gives rise to expressions for the gravity-wave contribution to bottom pressure, along with the expected acoustic–gravity wave contributions. Evanescent modes are also derived, but later ignored, since their effects in the far field are negligible. Expressions for surface elevation are obtained – broken down into contributions from the surface wave and the acoustic–gravity waves. The form of the governing equations for the envelope factors involved in the long-range modulations are found to be identical for both acoustic–gravity waves and the surface wave, i.e. they both obey the Schrödinger equation. The addition of gravitation to the current model may have a beneficial effect on the accuracy achievable in the inverse theory calculations originally discussed in Mei & Kadri (2018), and further developed in Bernabe & Usama (2021). The second objective is to tackle a long-standing limitation which arises when applying a stationary-phase approximation. The derived explicit solution for the gravity mode (tsunami) is singular at the arrival time, which results in overlooking the main peak of the tsunami. To overcome this difficulty, we employ a multi-fault approach, where the original fault is split into stripes. Since each stripe has a different spatio-temporal singularity, the main tsunami amplitude can be reconstructed by superposition principle.

Extension to multi-fault ruptures arises naturally from the linear theory by application of the superposition principle, enabling fault systems such as that discussed in Hamling *et al.* (2017) to be investigated. Two instances of multi-faults are considered here, one based upon the 2011 Tohoku event (detailed data can be found in Abdolali *et al.* 2017) and the second is based on the Sumatra 2004 event.

In this paper, we explicitly ignore contributions from terms of second order and higher, (i.e. nonlinear terms) on wave amplitude over the spatial range of interest. In addition, we assume that the evolution of each acoustic mode does not involve mode coupling (Michele & Renzi 2020). This is well justified for acoustic–gravity waves that are the main focus of this work.

2. Governing equations

The water layer is assumed to be inviscid, homogeneous and of constant depth h. The origin of the Cartesian coordinates is located at the sea bottom, at the centroid of the fault, with the vertical axis z directed vertically upward. Based on irrotational flow, the problem is formulated in terms of the velocity potential $\varphi(x, y, z, t)$, where $\boldsymbol{u} = \nabla\varphi$ is the velocity field. Considering the slight compressibility of the sea, the velocity potential obeys the standard three-dimensional wave equation,

$$\frac{\partial^2\varphi}{\partial x^2} + \frac{\partial^2\varphi}{\partial y^2} + \frac{\partial^2\varphi}{\partial z^2} - \frac{1}{c^2}\frac{\partial^2\varphi}{\partial t^2} = 0, \tag{2.1}$$

where c is the speed of sound in water. For the boundary condition at the free surface, we make use of results obtained from the detailed derivation given in Mei, Stiassnie & Yue (2009, § 1.1.2). We assume that (1) the wavelengths are long enough so that surface tension effects are negligible, (2) the atmospheric pressure is constant and (3) nonlinear terms can be neglected over the spatial region of interest. Then with g taken to be the acceleration due to gravity the linearised, combined dynamic and kinematic boundary condition is

$$\frac{\partial^2\varphi}{\partial t^2} + g\frac{\partial\varphi}{\partial z} = 0. \tag{2.2}$$

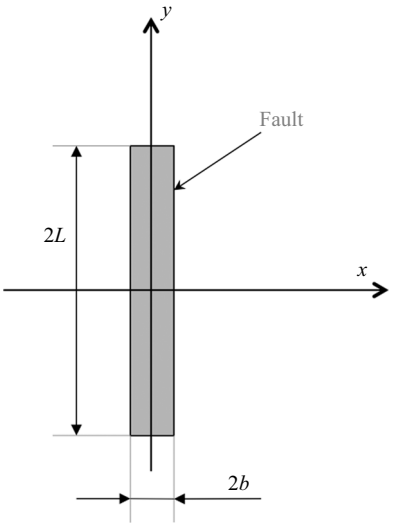

Figure 1. Sketch of slender fault.

Following Mei & Kadri (2018), the fault's ground motion is confined to a rigid, slender rectangular stripe of width $2b$ and length $2L$, with a slenderness parameter $\varepsilon = b/L \ll 1$ (see figure 1), such that

$$\frac{\partial \varphi}{\partial z} = w(x, y)\tau(t), \quad z = 0, \tag{2.3}$$

where

$$w(x, y) = \begin{cases} W_0 = \text{const} & |x| < b, \quad |y| < L \\ 0 & \text{elsewhere} \end{cases}, \quad \tau(t) = \begin{cases} 1 & -T < t < T \\ 0 & |t| > T \end{cases}, \quad (z = 0). \tag{2.4a,b}$$

where $w(x, y)$ defines the spatial extent of the rupture, τ defines the time the rupture is active (rupture duration $= 2T$) and W_0 is the uplift velocity. To study the long-distance propagation of acoustic–gravity waves, we introduce re-scaled coordinates (see Mei & Kadri 2018)

$$X = \varepsilon^2 x, \quad Y = \varepsilon y. \tag{2.5a,b}$$

Letting $\varphi = \varphi_0(x, X, Y, z, t) + \varepsilon^2 \varphi_2(x, X, Y, z, t) + \cdots$ where φ_0 and φ_2 represent the leading order and second order velocity potentials, respectively, the potential reduces to the two-dimensional wave equation to leading order,

$$\frac{\partial^2 \varphi_0}{\partial x^2} + \frac{\partial^2 \varphi_0}{\partial z^2} - \frac{1}{c^2}\frac{\partial^2 \varphi_0}{\partial t^2} = 0, \tag{2.6}$$

with boundary conditions given by,

$$\frac{\partial^2 \varphi_0}{\partial t^2} + g\frac{\partial \varphi_0}{\partial z} = 0, \quad (z = h) \tag{2.7}$$

$$\frac{\partial \varphi_0}{\partial z} = \begin{cases} W_0\tau(t) & |x| < b, \quad |y| < L \\ 0 & \text{elsewhere} \end{cases}, \quad \tau(t) = \begin{cases} 1 & -T < t < T \\ 0 & |t| > T \end{cases}, \quad (z = 0). \tag{2.8a,b}$$

The envelope of the radiated waves is governed by

$$\frac{\partial^2\varphi_2}{\partial x^2}+\frac{\partial^2\varphi_2}{\partial z^2}-\frac{1}{c^2}\frac{\partial^2\varphi_2}{\partial t^2}=-\left[\frac{\partial^2\varphi_0}{\partial Y^2}+2\frac{\partial^2\varphi_0}{\partial x\partial X}\right], \tag{2.9}$$

with the boundary conditions,

$$\frac{\partial^2\varphi_2}{\partial t^2}+g\frac{\partial\varphi_2}{\partial z}=0, \quad (z=h) \tag{2.10}$$

$$\frac{\partial\varphi_2}{\partial z}=0, \quad (z=0). \tag{2.11}$$

Note that the boundary conditions for φ_0 and φ_2 at $z=h$ here are different to those in the 'no-gravity' case ($\varphi_0=\varphi_2=0$).

3. Solution

3.1. *Leading order*

Utilising a double Fourier transform $\Phi=\int_{-\infty}^{\infty}\int_{-\infty}^{\infty}\varphi_0\exp(-\mathrm{i}(kx-\omega t))\,\mathrm{d}t\,\mathrm{d}x$, with ω representing angular velocity and k the wavenumber, the transformed potential is found to be

$$\Phi=\frac{4W_0\sin(kb)\sin(\omega T)}{\mu k\omega}\left\{\frac{\mu g\cos\left[\mu(h-z)\right]-\omega^2\sin\left[\mu(h-z)\right]}{\left[\omega^2\cos(\mu h)+\mu g\sin(\mu h)\right]}\right\}, \tag{3.1}$$

where $\mu^2=(\omega^2/c^2)-k^2$. The poles contributing to the contour integration derive from the dispersion relation $\omega^2\cos(\mu h)+\mu g\sin(\mu h)=0$ in the denominator of (3.1). The first eigenvalue μ_0 is imaginary – all the rest are real. The first wavenumber k_0 corresponding to a gravity wave is always real. The following $n\leq N$ wavenumbers $[k_1,k_2,\ldots,k_N]$ are also real, and correspond to the acoustic–gravity waves where $N=\lfloor(\omega h/\pi c)+1/2\rfloor$. The gravity and acoustic–gravity modes are progressive waves. The next modes, $n>N$ with wavenumbers λ_n correspond to decaying, evanescent modes (Kadri & Stiassnie 2012). Thus, all modes satisfy the dispersion relation where

$$k_0=\sqrt{\frac{\omega^2}{c^2}+\mu_0^2}, \quad k_n=\sqrt{\frac{\omega^2}{c^2}-\mu_n^2}, \quad \lambda_n=\sqrt{\mu_n^2-\frac{\omega^2}{c^2}}. \tag{3.2a–c}$$

Inverting the transformation by contour integration, we obtain the velocity potential,

$$\begin{aligned}\varphi_0=&-\frac{W_0}{\pi}\mathrm{Re}\int_0^{\infty}\mathrm{i}\mathrm{d}\omega\frac{8\mu_0\sin(k_0b)\sin(\omega T)\cosh(\mu_0 z)}{\omega k_0^2\left[2\mu_0h+\sinh(2\mu_0h)\right]}\exp(\mathrm{i}(k_0|x|-\omega t))\\&-\frac{W_0}{\pi}\mathrm{Re}\int_{\omega_n}^{\infty}\mathrm{i}\mathrm{d}\omega\sum_{n=1}^{N}\frac{8\mu_n\sin(k_nb)\sin(\omega T)\cos(\mu_n z)}{\omega k_n^2\left[2\mu_nh+\sin(2\mu_nh)\right]}\exp(\mathrm{i}\,(k_n|x|-\omega t))\\&-\frac{W_0}{\pi}\int_0^{\omega_n}\mathrm{d}\omega\cos(\omega t)\sum_{n=N+1}^{\infty}\frac{8\mu_n\sinh(k_nb)\sin(\omega T)\cos(\mu_n z)}{\omega\lambda_n^2\left[2\mu_nh+\sin(2\mu_nh)\right]}\mathrm{e}^{-\lambda_n|x|}.\end{aligned} \tag{3.3}$$

where ω_n is given by $\omega_n=(n-\frac{1}{2})\frac{\pi c}{h}$.

Then picking out the real part for the propagating modes gives

$$\varphi_0 = \frac{8W_0}{\pi}\int_0^\infty \mathrm{d}\omega \frac{\mu_0 \sin(k_0 b)\sin(\omega T)\cosh(\mu_0 z)}{\omega k_0^2\left[2\mu_0 h + \sinh(2\mu_0 h)\right]}\sin(k_0|x| - \omega t) + \frac{8W_0}{\pi}\int_{\omega_n}^\infty \mathrm{d}\omega \sum_{n=1}^{N} \frac{\mu_n \sin(k_n b)\sin(\omega T)\cos(\mu_n z)}{\omega k_n^2\left[2\mu_n h + \sin(2\mu_n h)\right]}\sin(k_n|x| - \omega t)\,. \tag{3.4}$$

From which the pressure and surface elevation expressions can be obtained by differentiation using

$$P = -\rho\frac{\partial \varphi_0}{\partial t}, \quad \eta = -\frac{1}{g}\frac{\partial \varphi_0}{\partial t}. \tag{3.5a,b}$$

where ρ is liquid density and η the surface elevation. Thus the pressure terms are now given by

$$P = \frac{8\rho W_0}{\pi}\int_0^\infty \mathrm{d}\omega \frac{\mu_0 \sin(k_0 b)\sin(\omega T)\cosh(\mu_0 z)}{k_0^2\left[2\mu_0 h + \sinh(2\mu_0 h)\right]}\cos(k_0|x| - \omega t) + \frac{8\rho W_0}{\pi}\int_{\omega_n}^\infty \mathrm{d}\omega \sum_{n=1}^{N} \frac{\mu_n \sin(k_n b)\sin(\omega T)\cos(\mu_n z)}{k_n^2\left[2\mu_n h + \sin(2\mu_n h)\right]}\cos(k_n|x| - \omega t)\,, \tag{3.6}$$

with surface elevation terms given by

$$\eta = \frac{8W_0}{g\pi}\int_0^\infty \mathrm{d}\omega \frac{\mu_0 \sin(k_0 b)\sin(\omega T)\cosh(\mu_0 h)}{k_0^2\left[2\mu_0 h + \sinh(2\mu_0 h)\right]}\cos(k_0|x| - \omega t) + \frac{8W_0}{g\pi}\int_{\omega_n}^\infty \mathrm{d}\omega \sum_{n=1}^{N} \frac{\mu_n \sin(k_n b)\sin(\omega T)\cos(\mu_n h)}{k_n^2\left[2\mu_n h + \sin(2\mu_n h)\right]}\cos(k_n|x| - \omega t)\,. \tag{3.7}$$

The expressions for pressure and surface elevation are in agreement with Stiassnie (2010, (3.13) and (3.14)).

3.2. *Long-range modulation*

Considering the region far from the fault, Mei & Kadri (2018) showed that for pure acoustic modes the envelopes $A_n(X, Y)$ vary slowly, allowing the derivation of an analytical solution of the pressure. It is anticipated that the addition of gravity would have a similar effect where the modal envelopes of both the acoustic–gravity modes (with the correction due to gravity) and the gravity mode (with correction due to compressibility) are all governed by the Schrödinger equation, which once solved explicitly we obtain

$$A_n = \frac{1-\mathrm{i}}{2}\left\{C\left(\sqrt{\frac{2}{\pi\chi_n}}\mathcal{Y}_+\right) + C\left(\sqrt{\frac{2}{\pi\chi_n}}\mathcal{Y}_-\right)\right\} + \frac{1+\mathrm{i}}{2}\left\{S\left(\sqrt{\frac{2}{\pi\chi_n}}\mathcal{Y}_+\right) + S\left(\sqrt{\frac{2}{\pi\chi_n}}\mathcal{Y}_-\right)\right\}, \tag{3.8}$$

where $C(z)$ and $S(z)$ are Fresnel integrals and

$$\chi_n = X/2k_n, \quad \mathcal{Y}_\pm = (l \pm Y)/2. \tag{3.9a,b}$$

This result is identical in structure to that of Mei & Kadri (2018), though here it is valid also for the gravity mode $n = 0$. With the inclusion of these results for $A_n(k_n, X, Y)$, the leading order term for the velocity potential in (3.3) is now valid in the ranges $x \leq O(l\varepsilon^{-2}) = O(L\varepsilon^{-1})$, $y \leq O(l\varepsilon^{-1})$ where $l = \epsilon L$.

3.3. *Stationary-phase approximation*

We now apply the stationary-phase approximation for different gravity phase speed conditions. We rewrite (3.6) as

$$P = \frac{8\rho W_0}{\pi}\mathrm{Re}\int_0^\infty \mathrm{d}\omega \frac{\mu_0 \sin(k_0 b)\sin(\omega T)\cosh(\mu_0 z)}{k_0^2\left[2\mu_0 h + \sinh(2\mu_0 h)\right]}\exp \mathrm{i}\left(k_0|x| - \omega t\right)$$
$$+ \frac{8\rho W_0}{\pi}\mathrm{Re}\int_{\omega_n}^\infty \mathrm{d}\omega \sum_{n=1}^{N} \frac{\mu_n \sin(k_n b)\sin(\omega T)\cos(\mu_n z)}{k_n^2\left[2\mu_n h + \sin(2\mu_n h)\right]}\exp(\mathrm{i}\left(k_n|x| - \omega t\right)). \quad (3.10)$$

3.3.1. *Acoustic–gravity modes*

Consider the acoustic–gravity modes only, i.e. the second term in (3.10), and let the phase of mode n be denoted by $\Gamma_n(\omega)$, with

$$\Gamma_n(\omega) = k_n(\omega)\frac{x}{t} - \omega, \quad \text{where } k_n(\omega) = \frac{\sqrt{\omega^2 - \omega_n^2}}{c}. \quad (3.11)$$

A first derivative of $\Gamma_n(\omega)$ with respect to ω gives, at the point of stationary phase $\omega = \Omega_n$,

$$\Omega_n = \frac{\omega_n}{\sqrt{1 - \left(\dfrac{x}{ct}\right)^2}} \quad (3.12)$$

and a second derivative yields

$$k_n(\Omega_n) \equiv K_n = \frac{\sqrt{\Omega_n^2 - \omega_n^2}}{c} = \frac{\omega_n}{c}\frac{x/ct}{\sqrt{1 - \left(\dfrac{x}{ct}\right)^2}} \quad (3.13)$$

Applying the known stationary-phase formula, e.g. p. 539 of Richards (2009), the contribution to the pressure arising from the acoustic–gravity waves becomes

$$p_a = \sum_{n=1}^{N} \frac{\rho W_0}{\pi}|A_n|\frac{8\mu_n \sin(K_n b)\sin(\Omega_n T)\cos(\mu_n z)}{K_n^2\left[2\mu_n h + \sin(2\mu_n h)\right]}\left[\frac{2\pi}{\dfrac{x}{c}\dfrac{\omega_n^2}{\left(\Omega_n^2 - \omega_n^2\right)^{3/2}}}\right]^{1/2}$$
$$\times \cos\left(K_n|x| - \Omega_n t - \frac{\pi}{4} + \Theta_{An}\right), \quad (3.14)$$

where Θ_{An} is the phase of A_n. The results for the acoustic–gravity modes are consistent with the results for the (pure) acoustic modes by Mei & Kadri (2018) with the difference that the modes here have a correction due to gravity.

3.3.2. *Gravity–acoustic mode*

To obtain the stationary-phase approximation for the contribution to bottom pressure arising from the surface gravity wave – the first term in (3.10) – consider the phase term $\Gamma_0(\omega)$ for the general (compressible) case as given by

$$\Gamma_0(\omega) = k_0(\omega)\frac{x}{t} - \omega, \quad \Gamma_0'(\omega) = k_0'(\omega)\frac{x}{t} - 1 = 0, \quad \Gamma_0''(\omega) = k_0''(\omega)\frac{x}{t}, \tag{3.15a–c}$$

where single and doubles primes denote first and second derivatives with respect to ω. Noting that

$$k_0^2 = \frac{\omega^2}{c^2} + \mu_0^2, \quad k_0 = k_0(\omega) \quad \text{and} \quad \mu_0 = \mu_0(\omega), \tag{3.16}$$

differentiation with respect to ω yields

$$k_0' = \frac{1}{k_0}\left(\frac{\omega}{c^2} + \mu_0\mu_0'\right). \tag{3.17}$$

The stationary-phase approximation requires a second derivative of k_0,

$$k_0''(\omega) = \frac{1}{k_0}\left(\frac{1}{c^2} + \left(\mu_0'\right)^2 + \mu_0\mu_0''\right) - \frac{1}{k_0^2}\left(\frac{\omega}{c^2} + \mu_0\mu_0'\right)k_0'. \tag{3.18}$$

Equation (3.18) contains terms in μ_0' and μ_0''; to obtain these, we differentiate the general gravity dispersion relation

$$\omega^2 = g\mu_0 \tanh(\mu_0 h) \tag{3.19}$$

which gives

$$\widetilde{\mu_0}' = \frac{2\tilde{\omega}\tilde{\mu}_0}{\tilde{\omega}^2 + \widetilde{\mu_0}^2 - \tilde{\omega}^4}; \quad \widetilde{\mu_0}'' = \frac{\widetilde{\mu_0}'}{\tilde{\omega}} - \frac{(\widetilde{\mu_0}')^3}{\tilde{\omega}}\left(1 - \tilde{\omega}^2 - \frac{\tilde{\omega}^4}{\mu_0}^2 + \frac{\tilde{\omega}^6}{\widetilde{\mu_0}^2}\right) \tag{3.20a,b}$$

where, for simplicity, quantities with tilde were normalised with length scale h and time scale $\sqrt{h/g}$.

Following Richards (2009) and with $\omega = \Omega_0$ at the point of stationary phase, the pressure contribution arising from the surface gravity wave is given by

$$p_g = \frac{\rho W_0}{\pi}|A_0|\frac{8\mu_0 \sin(K_0 b)\sin(\Omega_0 T)\cosh(\mu_0 z)}{K_0^2\left[2\mu_0 h + \sinh(2\mu_0 h)\right]}\left[\frac{2\pi}{t\Gamma_0''(\Omega_0)}\right]^{1/2} \times \cos\left(K_0 x - \Omega_0 t + \frac{\pi}{4} + \Theta_{A0}\right), \tag{3.21}$$

where Θ_{A0} is the phase of A_0, and $\mu_0 \neq K_0$ in this case.

For the total pressure contribution from the propagating modes, we combine (3.14) with (3.21) to give

$$P(x,y,z,t) = \frac{\rho W_0}{\pi}|A_0|\frac{8\mu_0 \sin(K_0 b)\sin(\Omega_0 T)\cosh(\mu_0 z)}{K_0^2\left[2\mu_0 h + \sinh(2\mu_0 h)\right]} \times \left[\frac{2\pi}{t\Gamma_0''(\Omega_0)}\right]^{1/2} \cos\left(K_0 x - \Omega_0 t + \frac{\pi}{4} + \Theta_{A0}\right) + \sum_{n=1}^{N} \frac{\rho W_0}{\pi}|A_n|\frac{8\mu_n \sin(K_n b)\sin(\Omega_n T)\cos(\mu_n z)}{K_n^2\left[2\mu_n h + \sin(2\mu_n h)\right]} \left[\frac{2\pi}{\frac{x}{c}\frac{\omega_n^2}{\left(\Omega_n^2 - \omega_n^2\right)^{3/2}}}\right]^{1/2} \times \cos\left(K_n|x| - \Omega_n t - \frac{\pi}{4} + \Theta_{An}\right). \tag{3.22}$$

Similarly, the surface elevation terms become

$$\eta(x,y,z,t) = \frac{W_0}{g\pi}|A_0|\frac{8\mu_0 \sin(K_0 b)\sin(\Omega_0 T)\cosh(\mu_0 h)}{K_0^2\left[2\mu_0 h + \sinh(2\mu_0 h)\right]} \times \left[\frac{2\pi}{t\Gamma_0''(\Omega_0)}\right]^{1/2} \cos\left(K_0 x - \Omega_0 t + \frac{\pi}{4} + \Theta_{A0}\right) + \sum_{n=1}^{N} \frac{W_0}{g\pi}|A_n|\frac{8\mu_n \sin(K_n b)\sin(\Omega_n T)\cos(\mu_n h)}{K_n^2\left[2\mu_n h + \sin(2\mu_n h)\right]} \left[\frac{2\pi}{\frac{x}{c}\frac{\omega_n^2}{\left(\Omega_n^2 - \omega_n^2\right)^{3/2}}}\right]^{1/2} \times \cos\left(K_n x - \Omega_n t - \frac{\pi}{4} + \Theta_{An}\right) \tag{3.23}$$

The forms of $\Gamma_0''(\Omega_0)$, Ω_0 and K_0 are dependent upon any assumptions made as detailed in the three cases considered below: (1) a general solution with the compressible dispersion relation (3.19), (2) an approximate high-order dispersion relation and (3) first-order shallow-water approximation. The latter two assume incompressibility. Note that for brevity cases 2 and 3 are presented in non-dimensional form.

Case 1: Compressible gravity dispersion relation

Evaluation of the surface gravity wave contribution to surface elevation requires a method of calculation for μ_0, Ω_0, K_0 and Γ_0''. To obtain μ_0, we differentiate the general dispersion relation (3.19) with respect to k_0, and make use of $\Gamma_0'(\omega) = 0$ at stationary phase, which gives

$$2\mu_0 \frac{x}{t}\sqrt{g\mu_0 \tanh(\mu_0 h)} - \left(g\mu_0 \tanh(\mu_0 h) + g\mu_0^2 h - g\mu_0^2 h \tanh^2(\mu_0 h)\right)\frac{\mathrm{d}\mu_0}{\mathrm{d}k_0} = 0, \tag{3.24}$$

where

$$\frac{\mathrm{d}\mu_0}{\mathrm{d}k} = \sqrt{1 + \frac{g}{\mu_0 c^2}\tanh(\mu_0 h)} - \frac{x}{\mu_0 c^2 t}\sqrt{g\mu_0 \tanh(\mu_0 h)}. \tag{3.25}$$

Equations (3.24) and (3.25) form an implicit relationship for μ_0, which can be solved numerically. Once μ_0 has been obtained, Ω_0 and K_0 can be derived directly from

$$\Omega_0 = \sqrt{g\mu_0 \tanh(\mu_0 h)} \quad \text{and} \quad K_0 = \sqrt{\mu_0^2 + \frac{\Omega_0^2}{c^2}} \tag{3.26a,b}$$

and

$$\Gamma_0''(\Omega_0) = K_0''(\Omega_0)\frac{x}{t} = \frac{\mu_0}{K_0}\mu_0'' + \frac{1}{K_0^3 c^2}(\Omega_0\mu_0' - \mu_0)^2\frac{x}{t}. \tag{3.27}$$

Equation (3.27) contains terms in μ_0' and μ_0''; these are obtained from (3.20*a*,*b*).

Case 2: Third-order incompressible dispersion relation

Neglecting the compressibility of the water we can set $\tilde{\mu}_0 = \tilde{k}_0$ in (3.19). Consideration of the first two terms in the Taylor expansion of $\tanh(\tilde{k}_0)$ results in explicit forms for $\tilde{\Omega}_0$, $\tilde{K}_0$ and $\tilde{\Gamma}_0''$:

$$\tilde{\Omega}_0 = \frac{1}{8\tilde{t}^2}\left[6\tilde{t}^2 - \frac{3}{2}\tilde{x}\left(\tilde{x} + \sqrt{8\tilde{t}^2 + \tilde{x}^2}\right)\right]^{1/2}\left(\tilde{x} + \sqrt{8\tilde{t}^2 + \tilde{x}^2}\right), \tag{3.28}$$

$$\tilde{K}_0(x,t) = \sqrt{\frac{3}{2}}\left(1 - \sqrt{1 - \frac{4}{3}\tilde{\Omega}_0^2}\right)^{1/2}, \tag{3.29}$$

$$\tilde{\Gamma}_0''(\tilde{\Omega}_0) = \frac{(6\tilde{\Omega}_0^2 + 9)(3 - 2\tilde{K}_0^2) - 27}{(3\tilde{K}_0 - 2\tilde{K}_0^3)\left(3 - 4\Omega_0^2\right)\left(\sqrt{9 - 12\tilde{\Omega}_0^2} - 3\right)}\frac{\tilde{x}}{\tilde{t}}. \tag{3.30}$$

Case 3: Shallow-water limit

In addition to the assumption of compressibility ($\tilde{\mu}_0 = \tilde{k}_0$), we consider the case of shallow water, i.e. $\tanh(\tilde{k}_0) = \tilde{k}_0$, which leads to

$$\tilde{\Omega}_0 = \tilde{K}_0 = \sqrt{2}\left(\frac{\tilde{t}}{\tilde{x}} - 1\right)^{1/2}, \quad \tilde{\Gamma}_0'' = \tilde{K}_0''\frac{\tilde{x}}{\tilde{t}} \tag{3.31a,b}$$

in agreement with Stiassnie (2010, (4.3*a*,*b*)). To reduce to the 2-D case (Stiassnie 2010), the contribution from the envelope A_0 is removed (i.e. by setting $A_0 = 1$). Note that there is a factor of two magnification in the amplitude as compared with Stiassnie (2010), which is believed to be due to a typographical error in Stiassnie (2010) (see full derivation in supplementary material available at https://doi.org/10.1017/jfm.2021.101).

4. Validation

For validation purposes, we use input parameters similar to those found in Mei & Kadri (2018) and Stiassnie (2010), and that are listed in table 1. The number of acoustic modes is set at $N = 10$. This was shown to be a 'reasonable choice' in Stiassnie (2010) and Kadri & Stiassnie (2012). The uplift velocity of 0.1 ms^{-1}, along with rupture duration of 10 s, implies a fault displacement of 1 m. Aside from comparison with Stiassnie (2010), further justification for using a duration of the order of tens of seconds can be found in Abdolali *et al.* (2017) and Grilli *et al.* (2013).

The current model is first validated against the theoretical solution for an infinitely distributed fault, proposed by Stiassnie (2010) and a 3-D numerical solver

Constant	Description	Value
g	Acceleration due to gravity	9.81 ms^{-1}
L	Fault half-length	400 km
b	Fault half-width	40 km
$2T$	Rupture duration	10 s
h	Water depth	4 km
ρ	Water density	1000 kgm^{-3}
c	Speed of sound in water	1500 ms^{-1}
W_0	Uplift velocity	0.1 ms^{-1}
N	Number of acoustic modes	10

Table 1. Constants and parameters used in validation of current model with gravity.

(Sammarco *et al.* 2013; Abdolali *et al.* 2015*b*). The later solves (2.1) with (2.2) at the surface, the movable bottom, representing the vertical uplift (2.3) and (2.4*a*,*b*), and an outgoing Sommerfeld boundary condition at the end of numerical domain. The undistributed fault length assumption for the first set of validations allows us to use the 3-D numerical solver on a vertical transect, which is computationally affordable. It allows the presence of the surface gravity waves and all available acoustic modes interacting with each other. The only constraint is the minimum grid resolution and time stepping, required for resolving the range of dominant frequencies. In this simulation, proper values are used to ensure the first 10 modes exist in the domain.

For the second set of validations, a single finite fault case is considered over a large 2-D domain. The validation is conducted between the current model and a 2-D numerical solver based on the mild-slope equation (MSE) for weakly compressible fluid, rigid bottom (Sammarco *et al.* 2013).

In the third case, a real-world multi-fault scenario is considered over a large domain, where the theory and the depth-integrated model are compared to prove the accuracy of the theory. Then simulation on a variable bed condition is conducted to highlight the missing processes (i.e. refraction and reflection) due to the presence of seamounts and trenches.

Note that the solution, proposed by Stiassnie (2010), is fast, but has constant depth limit with an infinitely long fault assumption (2-D model). The current theory allows analysis of a single fault with finite longitudinal extent, and through linear superposition multi-fault conditions can also be investigated. On the other hand, the 3-D numerical solver is computationally expensive, but can take into account the entire problem without any assumption (i.e. variable depth profile). It is manageable to run it on transects, but requires massive computational resources for large 3-D domains with the necessary resolution to resolve the acoustic–gravity wave field. The depth-integrated model is faster than the 3-D solver, but still much slower than the theoretical solution. In addition, it requires the forcing to be decomposed and solved on spectral bands. Here, the validations are performed to prove the accuracy of each of the aforementioned models and theories, with proper overlaps. In other words, a coherent chain of cross-validation is performed to highlight the advantages of each method and the differences if assumptions are considered.

4.1. *Bottom pressure*

Consider a hydrophone station located at 1000 km along the positive x-axis. With the speed of sound fixed at 1500 ms^{-1}, the arrival time of the acoustic–gravity wave is

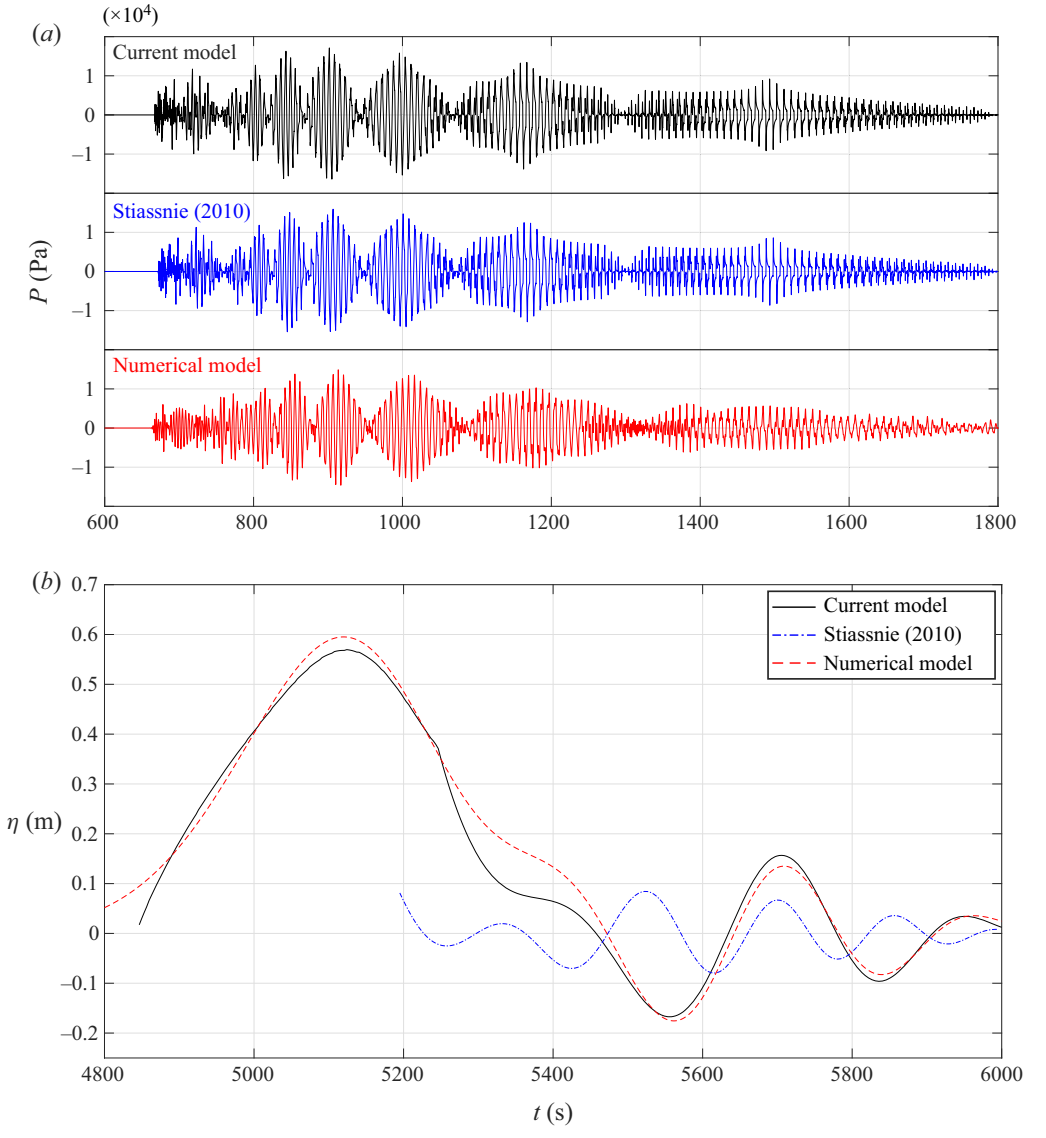

Figure 2. Comparison of current model against numerical model and Stiassnie (2010). (*a*) Bottom pressure signals predicted by current model (top), Stiassnie (2010) (middle) and numerical model (bottom). Coordinates are $x = 1000$, $y = 0$ km. (*b*) Surface elevation plots generated by current model (stationary-phase approximation inclusive of compressibility), Stiassnie (2010) and the numerical model. Coordinates are $x = 1000$, $y = 0$ km.

approximately 670 s after the rupture. The tsunami arrives later at around 5000 s. Figure 2(*a*) compares the bottom pressure signature calculated by the current model (top trace), Stiassnie (2010) (middle trace) and a 3-D numerical solver, which solves (2.1) with proper boundary conditions at the surface and end of the numerical domain and movable bottom (bottom trace).

4.2. *Surface elevation*

With the inclusion of gravitational effects into the current model, it is now possible to obtain surface elevation information in addition to the bottom pressure. Thus, the surface elevation results of figure 2(*b*) constitute new findings for the current model. This is of consequence when considering the inverse problem (Bernabe & Usama 2021), since it enables evaluation of the tsunami alongside the acoustic modes, thereby reducing computation time. A remarkable correction of the tsunami amplitude is obtained (black curve) by deserting the shallow water assumption suggested by Stiassnie (2010), and instead solving the full compressible dispersion relation for μ_0, Ω_0 and K_0 numerically. To illustrate this improvement, a comparison with a full numerical solution is presented (dashed red curve). Thus, an inclusion of compressibility in the tsunami calculations provides an important correction of the amplitude and frequency (Abdolali & Kirby 2017; Abdolali *et al.* 2019). It is also worth noting that an accurate gravity constant should be used.

At times approaching the critical time $\tilde{t}_c = \tilde{x}$, the solution is not valid, due to constraints arising from the limitations of the method of stationary phase and approximations made in calculating stationary points (Stiassnie 2010). In this case, the numerical model predicts a tsunami of peak amplitude approximately 0.6 m arriving at the critical time $\tilde{t}_c$. Unfortunately, all of the analytic models have a singularity at times approaching the critical time, see (3.23). However, by splitting up the fault into a few parallel stripes (say over 10), each stripe has a shift in the critical time which allows calculating the contribution of most of the fault at all times. Thus, the general compressible solution can capture the main peak at $\tilde{t}_c$ – see figure 2(*b*), which serves to further validate the linear multi-fault approach.

4.3. *Theoretical solution vs MSE*

In the previous section, the theoretical solutions for bottom pressure (3.22) have been validated against Stiassnie (2010) where the solutions exist for an infinite fault problem ($y = 0$). Here, the bottom pressure, calculated by the theory, is validated against numerical simulations based on the MSE for weakly compressible fluids (Sammarco *et al.* 2013), not only for points lying on the x-axis, but also for $y \neq 0$. The results are shown in figure 3 for a fault with dimensions of $L = 100$, $b = 10$ km and rise time of $2T = 10$ s, with residual displacement of $\zeta = 1$ m. As y increases, especially for $y \gg L$, the signals become smaller as expected (see the pressure field animation in the supplementary materials).

5. Multi-fault rupture

Hamling *et al.* (2017) discussed a fault that occurred on 14th November 2016 in Kaikōura, New Zealand. This event was reported as a 'complex multi-fault rupture' – complex in the sense that at least 12 major crustal faults and extensive uplift along much of the coastline were observed. The rupture jumped between faults located up to 15 km away from each other, and individual subfaults showed both positive and negative displacements as well as translational slipping.

The theory developed in § 3 is extended here to more complex situations, where two (or more), slender faults can be combined by linear superposition. Each fault may have its own uplift duration and velocity, as well as dimension and orientation. To take account of multiple faults relative to a reference time and location, the acoustic–gravity wave

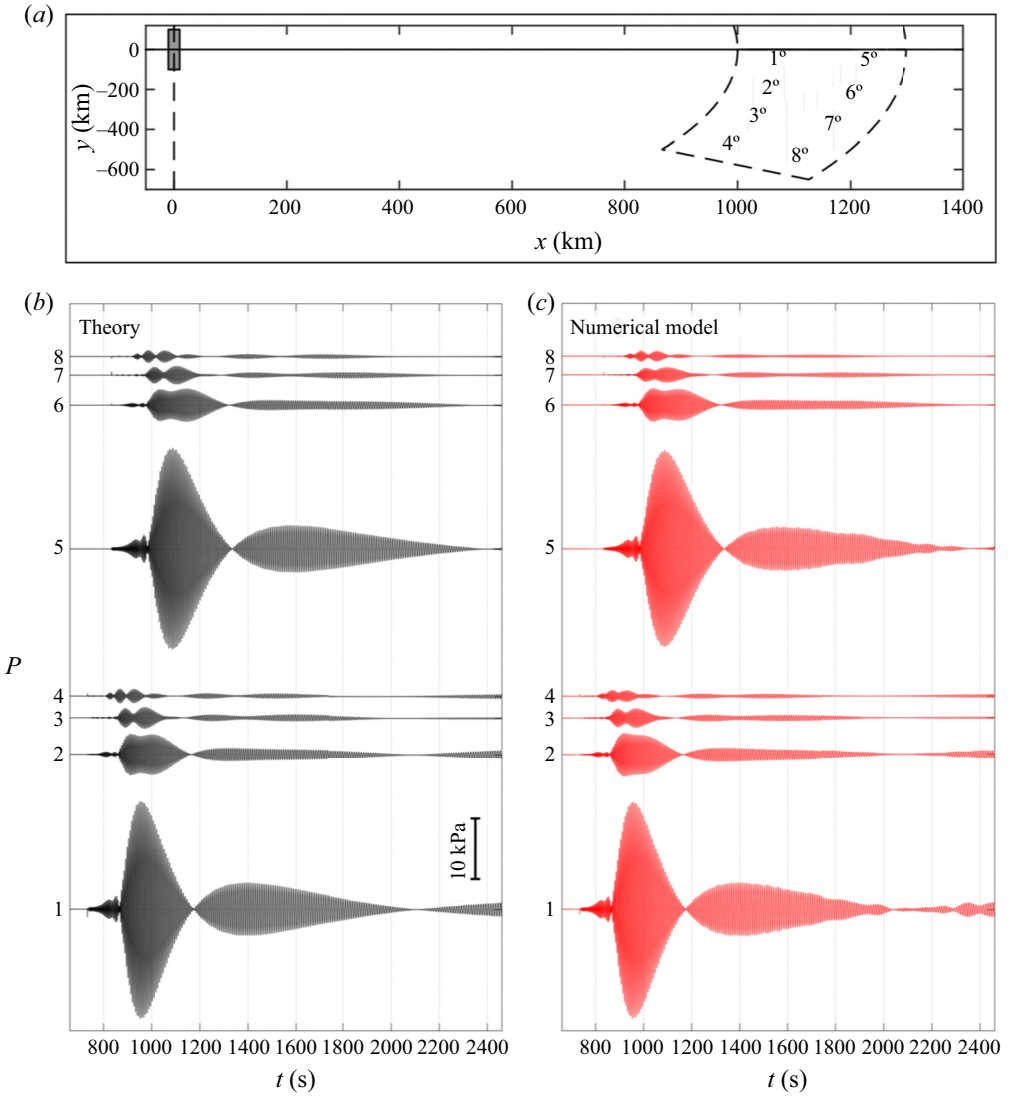

Figure 3. Panel (*a*) indicates the fault dimensions ($L = 100$ and $b = 10$ km), the numerical domain extent and the coordinates of the virtual point observations. The time series of bottom pressure calculated from the current model (*b*) and extracted from the numerical model (*c*). Only the first mode is considered in order to keep computation time manageable.

component of expression (3.22) is modified as

$$P = \sum_{i=1}^{M}\sum_{n=1}^{N} \frac{\rho W_{0,i}}{\pi}|A_{i,n}| \frac{8\mu_n \sin(K_{i,n}b_i)\sin(\Omega_{i,n}T_i)\cos(\mu_n z)}{K_{i,n}^2\,[2\mu_n h + \sin(2\mu_n h)]} \left[\frac{2\pi}{\dfrac{x_i}{c}\dfrac{\omega_n^2}{\left(\Omega_{i,n}^2 - \omega_n^2\right)^{3/2}}}\right]^{1/2}$$

$$\times \cos\left(K_{i,n}|x| - \Omega_{i,n}t(\bar{t}) - \frac{\pi}{4} + \Theta_{A_{i,n}}\right), \tag{5.1}$$

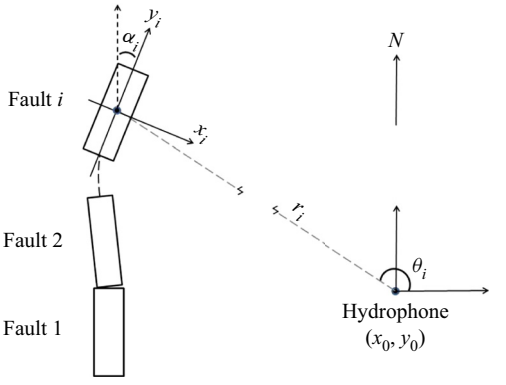

Figure 4. Location and orientation of a slender fault cluster relative to a hydrophone – axes and orientation of the ith fault indicated.

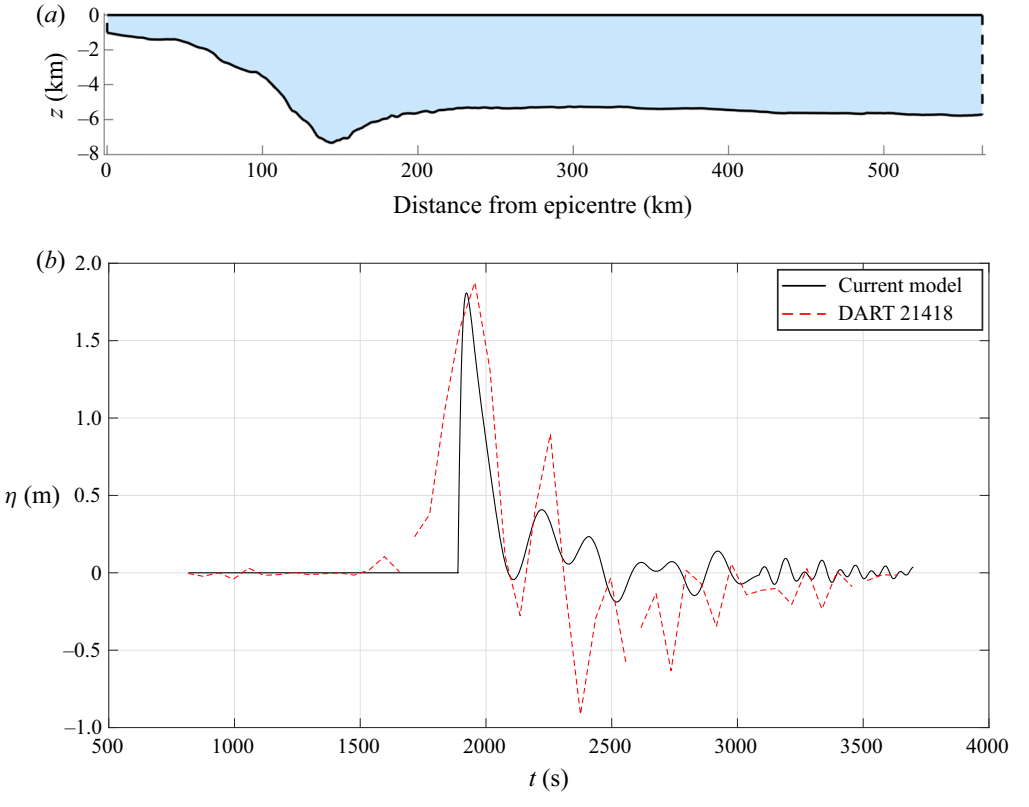

Figure 5. Comparison of current model against observation during Tohoku 2011. (*a*) Depth transect between Tohoku epicentre and DART buoy 21418. (*b*) Surface elevation comparison between current model (general compressible) and data recorded by DART buoy 21418 (red trace) for Tohoku 2011 event.

where i indexes the faults up to a maximum of M faults and $t(\bar{t})$ is defined as

$$t(\bar{t}) = H(\bar{t} - \Delta_i)(\bar{t} - \Delta_i), \tag{5.2}$$

where H is the Heaviside step function, $\bar{t} = 0$ is the time of the first fault movement and Δ_i is the time lag for each individual fault relative to that of the first moving fault.

Constant	Description	Value
g	Acceleration due to gravity	9.81 ms^{-1}
L	Fault half-length	150 km
b	Fault half-width	75 km
$2T$	Rupture duration	90 s
h	Water depth	5277 m
c	Speed of sound in water	1500 ms^{-1}
ζ_0	Uplift	7 m
r	Distance from epicentre	496.6 km
θ	Angle to epicentre	183.555°
α	Strike angle of fault	−13°

Table 2. Constants and parameters used in the calculation of predicted surface elevation at DART buoy 21418 for Tohoku 2011 event.

Parameter	Fault 1,2	Fault 3,4	Fault 5,6	Fault 7,8	Fault 9,10
longitude	94.57°	93.90°	93.21°	92.60°	92.87°
latitude	3.83°	5.22°	7.41°	9.70°	11.70°
Δ	0 s	212 s	528 s	853 s	1213 s
L	110 km	75 km	195 km	75 km	175 km
b	65 km	65 km	60 km	47.5 km	47.5 km
$2T$	60 s	60 s	60 s	60 s	60 s
ζ odd	7.02 m	8.59 m	4.72 m	4.49 m	4.60 m
ζ even	−3.27 m	−3.84 m	−2.33 m	−2.08 m	−2.31 m
W_0 odd	0.1170 ms^{-1}	0.1432 ms^{-1}	0.0787 ms^{-1}	0.0748 ms^{-1}	0.0767 ms^{-1}
W_0 even	−0.0545 ms^{-1}	−0.0640 ms^{-1}	−0.0388 ms^{-1}	−0.0347 ms^{-1}	−0.0385 ms^{-1}
α	37°	12°	22°	4°	−10°

Table 3. Parameters used for Sumatra 2004 event – ten faults in total. Includes ζ – the vertical displacement.

Consider a hydrophone located on the seabed ($z = 0$) and to the right of a cluster of faults as shown in figure 4. Then the (x, y) location of the hydrophone in each fault's coordinate system is given by

$$x_i = -r_i \cos(\theta_i - \alpha_i), \quad y_i = -r_i \sin(\theta_i - \alpha_i). \tag{5.3a,b}$$

5.1. *Multi-fault examples*

Hamling *et al.* (2017) does not contain information on multi-fault geometries and timings, etc. that would facilitate a validation exercise, so to link the current model with real data refer to Grilli *et al.* (2007) and Abdolali *et al.* (2017). The first paper discusses the Sumatra 2004 tsunami, and we use this to investigate agreement between the developed theory and a numerical model for acoustic–gravity waves (constant and variable depth). Since the DART network was not available at that time, we could not reliably validate the surface wave using the Sumatra event. Satellite records of surface displacement are available for Sumatra 2004 (Gower 2005), but these vary in both time and space, as the satellite moves across the Indian Ocean, and thus introduce unnecessarily delicate challenges. Instead, we opted to use the Tohoku 2011 event (Abdolali *et al.* 2017) as reference for the surface-wave validation where reliable data via the DART network is available. The DART buoys benefit from being at fixed locations while recording their time series of surface elevations.

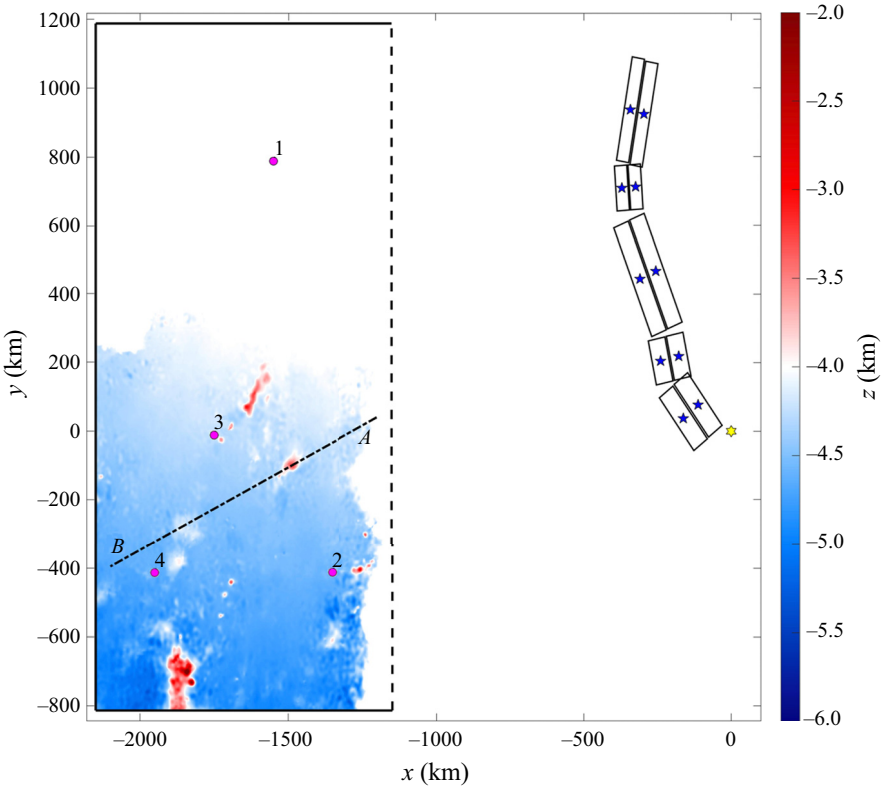

Figure 6. Overview of area considered for the bottom pressure map. The section to the left of the black dashed line is that used in the calculations for figure 8. The origin of x, y coordinates is at the earthquake epicentre (yellow star). Fault centroids are shown by blue stars and the faults delineated by rectangles. Depth below sea level is indicated by the colour bar with the white areas at 4 km depth. The four points used to construct the time series of figure 7 are labelled 1, 2, 3 and 4. The transect AB is shown with a dashed line.

5.1.1. *Tohoku 2011 – surface elevation*

Abdolali *et al.* (2017) investigated the surface gravity and acoustic–gravity wave fields produced by the megathrust Tohoku 2011 tsunamigenic event. The surface deflections generated by this event were recorded by the DART network deployed by NOAA (National Oceanic and Atmospheric Administration). The event occurred at 14:46 local time (Japan Standard Time (JST)) (Abdolali *et al.* 2017), with the tsunami waves arriving at DART buoy 21418 located at 38.735 N, 148.655 E (NOAA website) approximately 30 minutes later (Abdolali *et al.* 2017). This buoy lies at a distance of approximately 500 km east of the epicentre, and is a good candidate for testing the surface elevation predictions made by the current model (see Figure 5). The parameters used in the model were derived from a variety of sources. The dimensions of the fault were obtained from Encyclopædia Britannica (https://www.britannica.com/event/Japan-earthquake-and-tsunami-of-2011). The coordinates of DART buoy 21418 referenced to the epicentre were calculated using the Haversine formula. The depth used for the calculation was an average (constant) value derived from a Google Earth transect between the epicentre and the DART buoy location. The strike angle α was taken from Okal, Reymond & Hébert (2014), and finally the uplift and rupture duration were estimated using figure 3 of Abdolali *et al.* (2017). From this figure, it can be seen that the majority of the uplift had already occurred

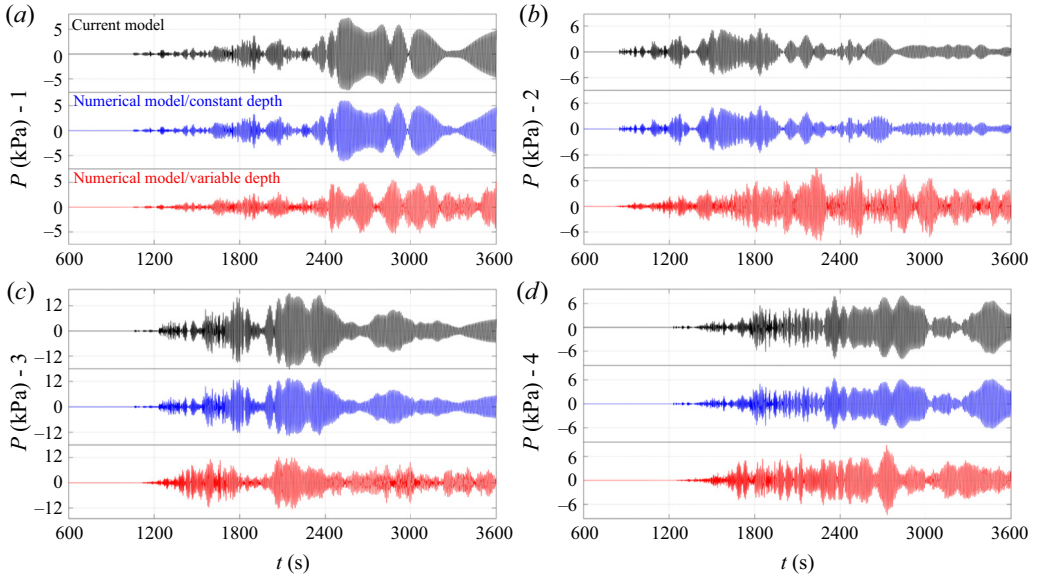

Figure 7. (*a–d*) Dynamic pressure time series for points 1, 2, 3 and 4 (from figure 6). The black trace is the current model (constant depth), the blue trace is a depth-integrated numerical model (constant depth) and the red trace is depth-integrated numerical but with variable depth.

by 90 s after t_0 – the start of the rupture. The maximum uplift was 11.35 m (Abdolali *et al.* 2017). Table 2 summarises the parameters used.

5.1.2. *Sumatra 2004 – acoustic–gravity waves*

Figures 7 and 8 present results of a comparison made between the (linear) current model and a depth-integrated numerical model applied to Sumatra 2004. Details of the parameters used in the model are summarised in table 3.

Computation of the bottom pressure field is for the region to the left of the dashed line shown in figure 6. Both the time series of figure 7 and the pressure maps of figure 8 demonstrate agreement between theory and numerics at constant depth (see the pressure field animation in the supplementary materials). Introduction of variable depth leads to the expected discrepancies between theory and the numerical model. However, even in the variable depth case, most of the important physics can be captured using the model. In figure 9, we can see the superposition of pressure signals emanating from multiple slender faults with differing orientations, resulting in areas of high pressure, and areas where the signal is weaker. The pressure contours of column three in figure 8 and the third column of figure 9 highlight the missing processes of refraction, diffraction and interference induced by the variable sea depth and areas of localised elevation (red coloured areas figure 6), with refraction dominating all modes in deep water (Renzi 2017). In figure 6, there is a transect with a seamount located approximately one third of the way along AB. The depth profile for this transect is shown at the top of figure 10. Also shown in figure 10 are pressure signals along the transect for three different times. The variable depth case (red trace) shows attenuation of the signal for points along the transect past 400 km (i.e. just after the seamount). This shadowing effect is also apparent in figure 9 where the seamount is to be found at approximately $x = -1500$, $y = -100$ km. More generally, acoustic–gravity waves propagating into shallow sea depth experience frequency filtering by the water

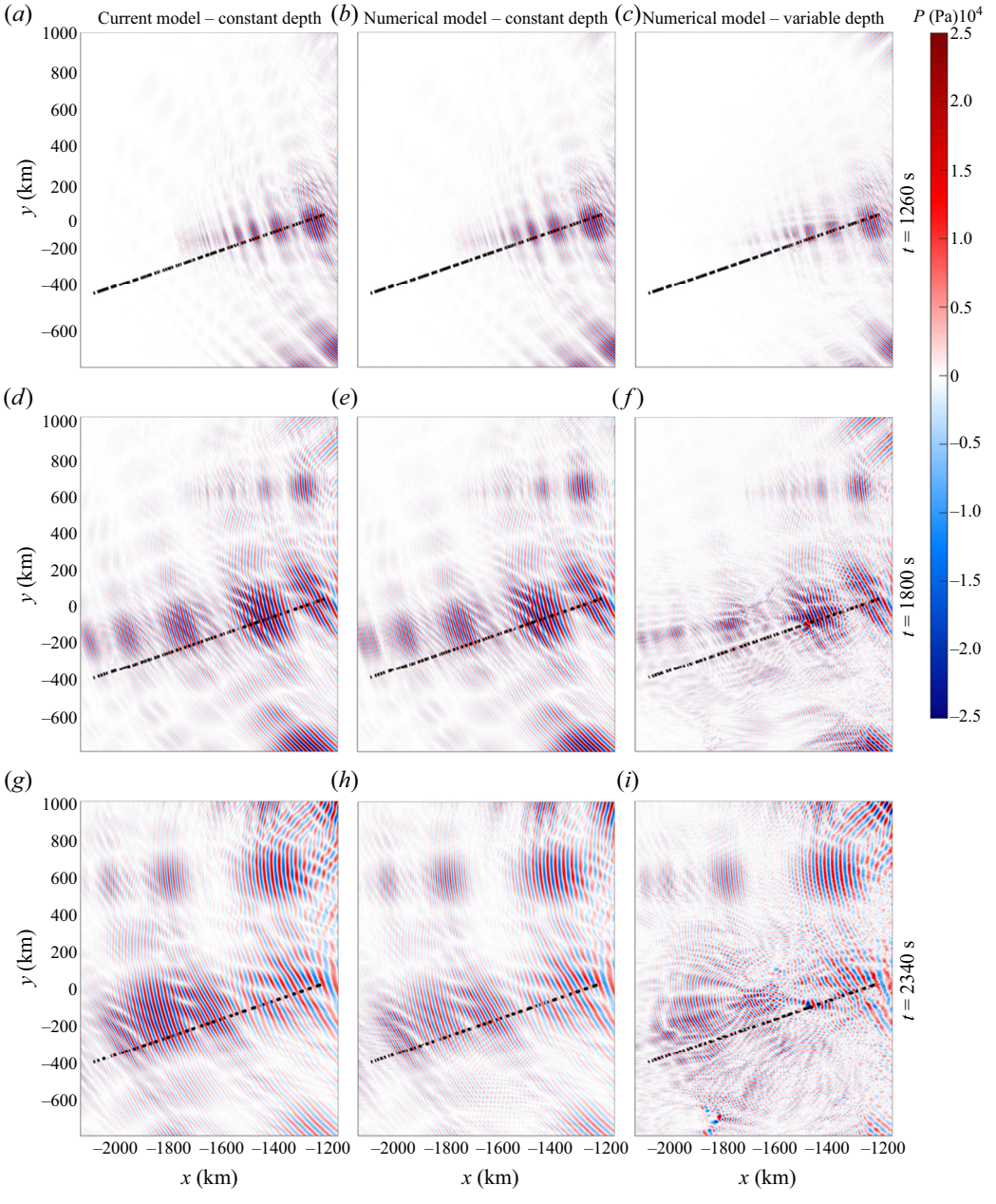

Figure 8. Snapshots of bottom pressure fields at $t = 1260$ s (*a–c*), $t = 1800$ s (*d–f*) and $t = 2340$ s (*g–i*) from the current model, (5.1) (*a*,*d*,*g*), numerical model for the case of constant depth of 4 km (*b*,*e*,*h*) and numerical model for the case of variable depth (*c*,*f* ,*i*). The domain extent is shown in figure 6 and the boundary forcing is imposed along the dashed line – also figure 6. The dynamic pressure variation is indicated with reference to the colour bar where white corresponds to 0 Pa. The transect AB is shown with dashed line in each subplot.

layer (Abdolali *et al.* 2015*a*; Cecioni *et al.* 2015). Low-order modes are associated with smaller critical depths and are therefore able to propagate further onshore (Abdolali *et al.* 2014; Renzi 2017). These results confirm that changing sea depth cannot be ignored when making these calculations, since it affects the timing and scale of the signals measurable

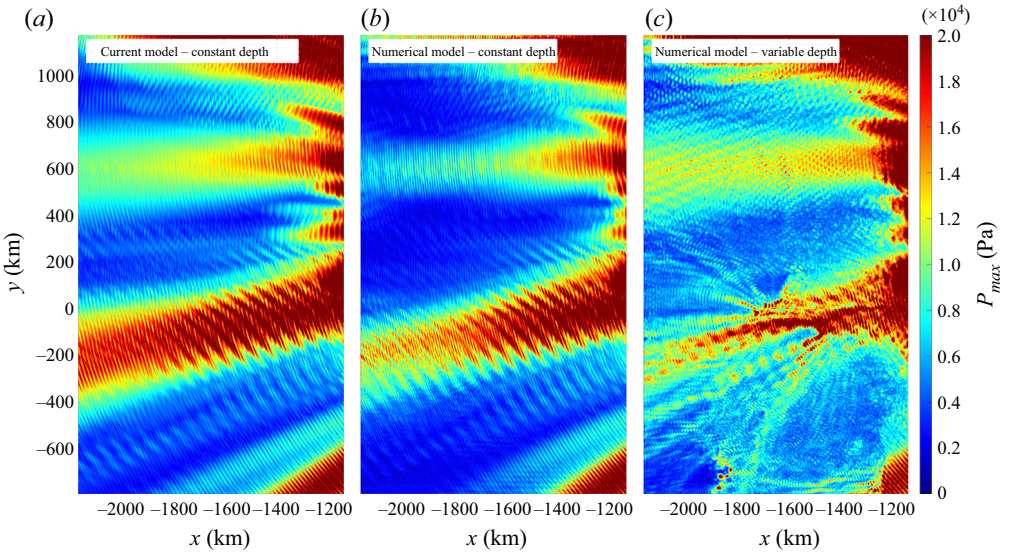

Figure 9. Maximum absolute values of the bottom pressure (P) of the acoustic wave generated by the Sumatra 2004 event during the first 1 h since rupture.

at any particular point. For instance, in the placement of hydrophones, the water should be of a depth so as to enable recording of a large frequency range (Abdolali *et al.* 2015*a*; Cecioni *et al.* 2015).

5.2. *Displacement function*

Aside from linear bottom displacement function (2.4*a*,*b*), the sensitivity of surface gravity and acoustic waves are investigated numerically for a half-sine (5.4) and an exponential (5.5) bottom displacement function (shown figure 11(*a*) (Hammack 1973)):

$$\zeta_s(x,y,t) = \zeta_0\left[\frac{1}{2}\left(1-\cos\frac{\pi t}{T}\right)H(T-t)+H(t-T)\right]H(b^2-x^2)H(L^2-y^2) \quad (5.4)$$

$$\zeta_e(x,y,t) = \zeta_0(1-\mathrm{e}^{-\alpha t})H(b^2-x^2)H(L^2-y^2), \quad (5.5)$$

where H is the Heaviside step function and ζ_0 is the residual displacement. For exponential displacement, $\zeta_e(t=T)=2\zeta_0/3$ or $T=1.11/\alpha$. The linear and exponential displacement functions result in very similar surface elevation plots, whereas their associated acoustic–gravity wave plots show a difference in amplitude, with the exponential displacement function delivering a smaller amplitude. The surface elevation predicted by the current model (general compressible) for a linear displacement function is also shown. The half-sine displacement function shows a marked difference in surface elevation amplitude when compared with either of the linear, or the exponential displacement functions – approximately 50 %. The half-sine displacement function is the only one of the three to have a smooth transition in velocity at $t=0$. The amplitude of the acoustic–gravity wave produced in this case ends up larger (by $t=1600$ s) than either of the linear or exponential cases, suggesting that energy is directed towards producing a larger acoustic–gravity wave at the expense of the surface wave.

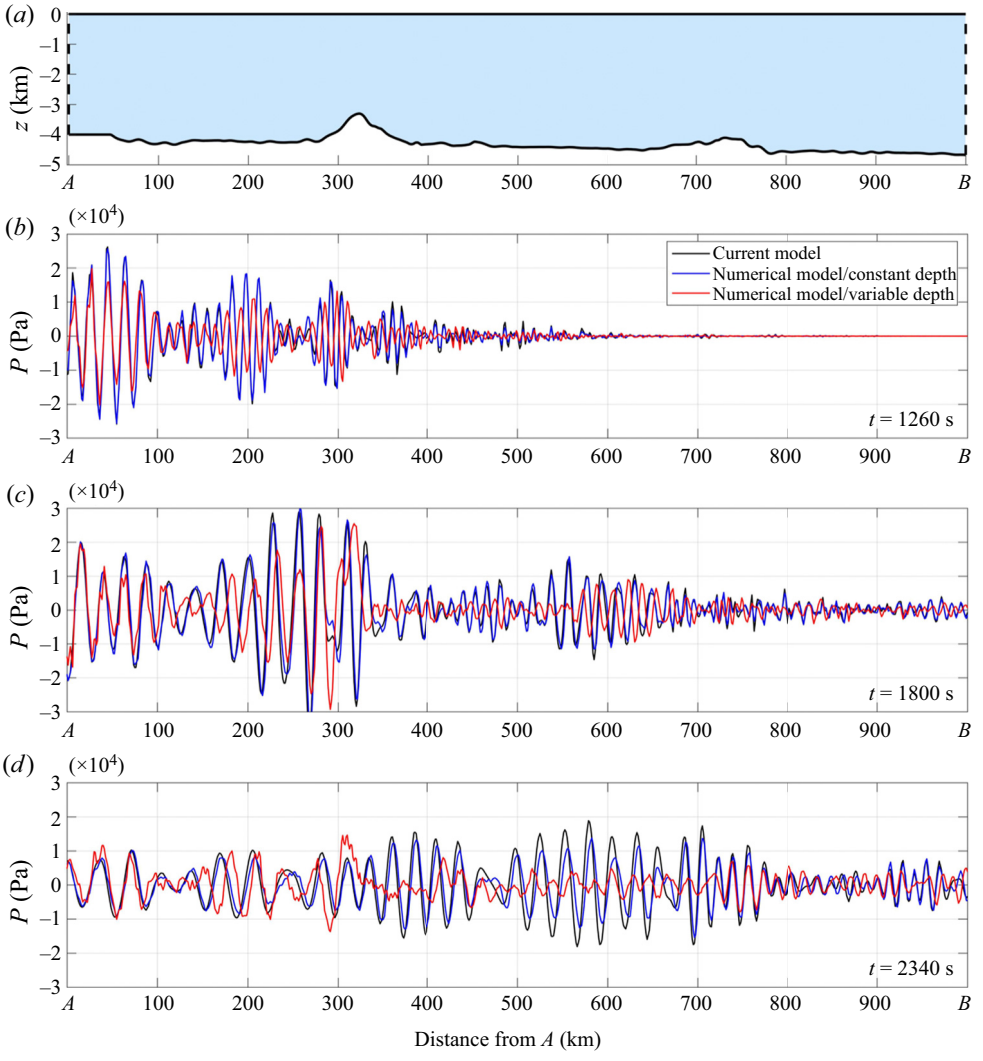

Figure 10. (*a*) The ocean profile along section AB (as shown in figures 6 and 8). (*b–d*) Bottom pressure anomalies along transect AB at $t = 1260$, 1800 and 2340 s from the current model (black), numerical model with constant depth (blue) and numerical model with variable depth (red).

6. Discussion

The separation of scales between acoustic and gravity waves indeed suggests analysing each wave type separately, as reported in literature. Such separation allows a comprehensive, but simplified, study compromising the accuracy only slightly. However, such compromise may lead to a twofold negative impact on the implementation of a reliable early tsunami warning system. The first is that reducing the uncertainties is critical in the inverse problem (Bernabe & Usama 2021), which can be done with the model without adversely affecting the calculation time. The second is that an inverse approach that employs pure acoustic theory only can initially provide properties of the fault, but then calculations of the rising tsunami need to be carried out. Our model enables simultaneous calculation of all acoustic–gravity modes, including the rising gravity mode (tsunami), thus minimising the calculation time.

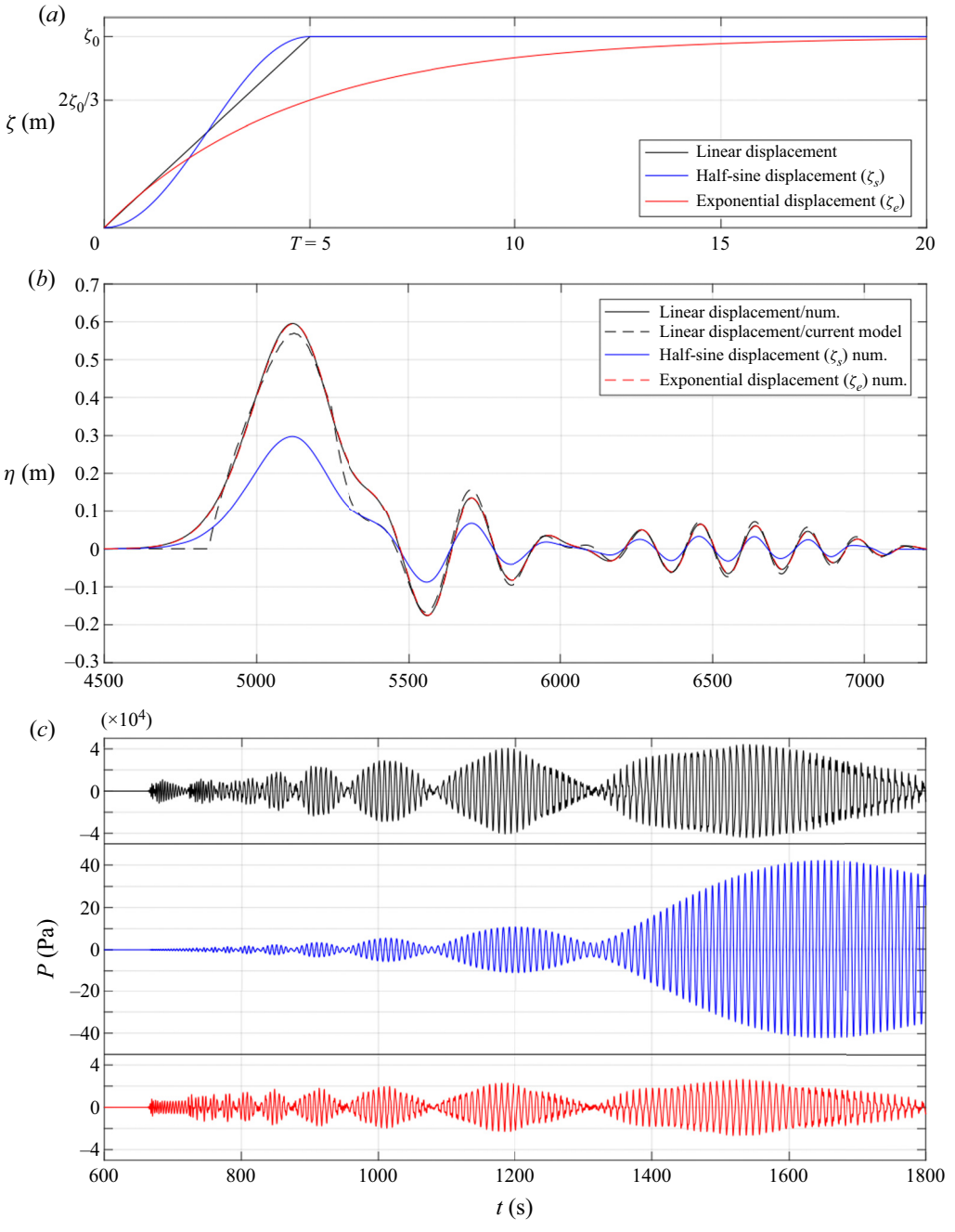

Figure 11. (*a*) The time series of bottom displacement for linear, half-sine (ζ_s) and exponential (ζ_e) functions. (*b*) The time series of surface elevation (η) and (*c*) bottom pressure signals. Coordinates are $x = 1000$, $y = 0$ km.

The current model includes a constant water-depth assumption, which has implications that cannot be ignored. While the model can estimate the tsunami in the deep water, it may not be effective in describing the propagation over varying bathymetry and the shelf break for two principal reasons. The first lies in the assumption of constant depth, and thus

effective techniques that take into account changes due to topography without computing the whole 3-D domain need to be developed. The second reason is the neglect of sea-floor elasticity, which turns out to be important for both tsunami and acoustic–gravity wave arrival times (Kadri 2019). For the tsunami, neglecting elasticity results in overestimation of the phase speed (Watada 2013; Watada, Kusumoto & Satake 2014; Abdolali *et al.* 2015*b*, 2018). The effect is even more dramatic for acoustic–gravity waves as they can couple to the elastic sea floor and travel at speeds reaching 3900 ms^{-1} which significantly changes their arrival time (Eyov *et al.* 2013).

Extensions to the existing model could be developed in many ways, one of which would be to address the assumption of constant sound speed. The work of Michele & Renzi (2020) highlighted the importance of including variable sound speed profiles into practical applications such as tsunami early warning. Another area in which the model may be improved lies in the assumption of an idealised rectangular geometry for the faults. Although table 1 of Mei & Kadri (2018) shows the rectangular fault assumption to be valid in many cases, it is obviously not valid for all. Future work could include the addition of dip and rake angles as parameters and also provision for the fault to rise with different velocities along its length, rather than the whole fault moving together with one set velocity.

Supplementary material and movies. Supplementary material and movies are available at https://doi.org/10.1017/jfm.2021.101.

Declaration of interests. The authors report no conflict of interest.

Author ORCIDs.
Byron Williams https://orcid.org/0000-0002-7489-9720;
Usama Kadri https://orcid.org/0000-0002-5441-1812;
Ali Abdolali https://orcid.org/0000-0003-3946-1552.

Author contributions. U.K. conceptualised the problem B.W. and U.K. derived the theory, A.A. developed the numerical model and B.W. and A.A. performed the simulations. All authors contributed equally to analysing data and reaching conclusions, and in writing the paper.

References

Abdolali, A., Cecioni, C., Bellotti, G. & Kirby, J.T. 2015*a* Hydro-acoustic and tsunami waves generated by the 2012 Haida Gwaii earthquake: modeling and in situ measurements. *J. Geophys. Res.* **120** (2), 958–971.

Abdolali, A., Cecioni, C., Bellotti, G. & Sammarco, P. 2014 A depth-integrated equation for large scale modeling of tsunami in weakly compressible fluid. *Coast. Engng Proc.* **1** (34), 9.

Abdolali, A., Kadri, U. & Kirby, J.T. 2019 Effect of water compressibility, sea-floor elasticity, and field gravitational potential on tsunami phase speed. *Sci. Rep.* **9**, 16874.

Abdolali, A., Kadri, U., Parsons, W. & Kirby, J.T. 2018 On the propagation of acoustic–gravity waves under elastic ice sheets. *J. Fluid Mech.* **837**, 640–656.

Abdolali, A. & Kirby, J.T. 2017 Role of compressibility on tsunami propagation. *J. Geophys. Res.* **122** (12), 9780–9794.

Abdolali, A., Kirby, J.T. & Bellotti, G. 2015*b* Depth-integrated equation for hydro-acoustic waves with bottom damping. *J. Fluid Mech.* **766**, R1.

Abdolali, A., Kirby, J.T., Bellotti, G., Grilli, S. & Harris, J.C. 2017 Hydro-acoustic wave generation during the Tohoku-Oki 2011 earthquake. In *Coastal Structures and Solutions to Coastal Disasters 2015*, pp. 24–34. American Society of Civil Engineers.

Bernabe, G. & Usama, K. 2021 Near real-time calculation of submarine fault properties using an inverse model of acoustic signals. *Appl. Ocean Res.* **109**, 102557.

Cecioni, C., Abdolali, A., Bellotti, G. & Sammarco, P. 2015 Large-scale numerical modeling of hydro-acoustic waves generated by tsunamigenic earthquakes. *Nat. Hazards Earth Syst. Sci.* **15** (3), 627–636.

CECIONI, C., BELLOTTI, G., ROMANO, A., ABDOLALI, A., SAMMARCO, P. & FRANCO, L. 2014 Tsunami early warning system based on real-time measurements of hydro-acoustic waves. *Procedia Engng* **70**, 311–320.

DZIEWONSHI, A.M. & ANDERSON, D.L. 1981 Preliminary earth reference model. *Phys. Earth Planet. Inter.* **25**, 297–356.

EYOV, E., KLAR, A., KADRI, U. & STIASSNIE, M. 2013 Progressive waves in a compressible-ocean with an elastic bottom. *Wave Motion* **50** (5), 929–939.

GOWER, J. 2005 Jason 1 detects the 26 December 2004 tsunami. *EOS Trans. AGU* **86** (4), 37–38.

GRILLI, S.T., HARRIS, J.C., TAJALLI BAKHSH, T.S., MASTERLARK, T.L., KYRIAKOPOULOS, C., KIRBY, J.T. & SHI, F. 2013 Numerical simulation of the 2011 Tohoku tsunami based on a new transient FEM Co-seismic source: comparison to far- and near-field observations. *Pure Appl. Geophys.* **170** (6–8), 1333–1359.

GRILLI, S.T., IOUALALEN, M., ASAVANANT, J., SHI, F., KIRBY, J.T. & WATTS, P. 2007 Source constraints and model simulation of the December 26, 2004, Indian Ocean tsunami. *ASCE J. Waterway Port Coastal Ocean Engng* **133** (6), 414–428.

HAMLING, I.J., *et al.* 2017 Complex multifault rupture during the 2016 M_w 7.8 Kaikōura earthquake, New Zealand. *Science* **356** (6334), eaam7194.

HAMMACK, J.L. 1973 A note on tsunamis: their generation and propagation in an ocean of uniform depth. *J. Fluid Mech.* **60** (4), 769–799.

HENDIN, G. & STIASSNIE, M. 2013 Tsunami and acoustic-gravity waves in water of constant depth. *Phys. Fluids* **25** (8), 086103.

KADRI, U. 2015 Acoustic-gravity waves interacting with a rectangular trench. *Intl J. Geophys.* **2015**, 1–9.

KADRI, U. 2016 Generation of hydroacoustic waves by an oscillating ice block in Arctic zones. *Adv. Acoust. Vib.* **2016**, 1–7.

KADRI, U. 2019 Effect of sea-bottom elasticity on the propagation of acoustic–gravity waves from impacting objects. *Sci. Rep.* **9** (1), 912.

KADRI, U. & AKYLAS, T.R. 2016 On resonant triad interactions of acoustic–gravity waves. *J. Fluid Mech.* **788**, R1.

KADRI, U. & STIASSNIE, M. 2012 Acoustic-gravity waves interacting with the shelf break: interaction of acoustic-gravity waves. *J. Geophys. Res.* **117** (C3), C03035.

KADRI, U. & STIASSNIE, M. 2013*a* Generation of an acoustic-gravity wave by two gravity waves, and their subsequent mutual interaction. *J. Fluid Mech.* **735**, R6.

KADRI, U. & STIASSNIE, M. 2013*b* A note on the shoaling of acoustic–gravity waves. *WSEAS Trans. Fluid Mech.* **8** (2), 43–49.

MEI, C.C. & KADRI, U. 2018 Sound signals of tsunamis from a slender fault. *J. Fluid Mech.* **836**, 352–373.

MEI, C.C., STIASSNIE, M. & YUE, D.K.-P. 2009 *Theory and Applications of Ocean Surface Waves*. World Scientific.

MICHELE, S. & RENZI, E. 2020 Effects of the sound speed vertical profile on the evolution of hydroacoustic waves. *J. Fluid Mech.* **883**, A28.

MIYOSHI, H. 1954 Generation of the tsunami in compressible water (Part I). *J. Oceanogr. Soc. Japan* **10** (1), 1–9.

NOSOV, M.A. 1999 Tsunami generation in compressible ocean. *Phys. Chem. Earth* B **24** (5), 437–441.

OKAL, E.A., REYMOND, D. & HÉBERT, H. 2014 From earthquake size to far-field tsunami amplitude: development of a simple formula and application to DART buoy data. *Geophys. J. Intl* **196** (1), 340–356.

PRESTININZI, P., ABDOLALI, A., MONTESSORI, A., KIRBY, J.T. & ROCCA, M.L. 2016 Lattice Boltzmann approach for hydro-acoustic waves generated by tsunamigenic sea bottom displacement. *Ocean Model.* **107**, 14–20.

RENZI, E. 2017 Hydro-acoustic frequencies of the weakly compressible mild-slope equation. *J. Fluid Mech.* **812**, 5–25.

RENZI, E. & DIAS, F. 2014 Hydro-acoustic precursors of gravity waves generated by surface pressure disturbances localised in space and time. *J. Fluid Mech.* **754**, 250–262.

RICHARDS, D. 2009 *Advanced Mathematical Methods with Maple 2 Part Set: Advanced Mathematical Methods with Maple 2 Part Paperback Set*, 1st edn. Cambridge University Press.

SAMMARCO, P., CECIONI, C., BELLOTTI, G. & ABDOLALI, A. 2013 Depth-integrated equation for large-scale modelling of low-frequency hydroacoustic waves. *J. Fluid Mech.* **722**, R6.

SELLS, C.C.L. 1965 The effect of a sudden change of shape of the bottom of a slightly compressible ocean. *Phil. Trans. R. Soc. Lond.* A **258** (1092), 495–528.

STIASSNIE, M. 2010 Tsunamis and acoustic-gravity waves from underwater earthquakes. *J. Engng Maths* **67** (1–2), 23–32.

WATADA, S. 2013 Tsunami speed variations in density-stratified compressible global oceans: tsunami speed in layered ocean. *Geophys. Res. Lett.* **40** (15), 4001–4006.

WATADA, S., KUSUMOTO, S. & SATAKE, K. 2014 Traveltime delay and initial phase reversal of distant tsunamis coupled with the self-gravitating elastic earth: delay and precursor of distant tsunami. *J. Geophys. Res.* **119** (5), 4287–4310.

YAMAMOTO, T. 1982 Gravity waves and acoustic waves generated by submarine earthquakes. *Intl J. Soil Dyn. Earthq. Engng* **1** (2), 75–82.